山地・河川・海岸系における物質動態に関する研究 (第3報)

AUTHOR(S):

中川, 一; 関口, 秀雄; 澤田, 豊明; 林, 泰一; 山下, 隆男; 上野, 鉄男; 武藤, 裕則; 馬場, 康之; 芹澤, 重厚

CITATION:

中川, 一 ...[et al]. 山地・河川・海岸系における物質動態に関する研究 (第3報). 京都大学防災研究所年報. C 2006, 49(C): 95-111

ISSUE DATE:

2006-04-01

URL:

http://hdl.handle.net/2433/26678

京都大学防災研究所年報 第 49 号 C 平成 18 年 4 月
Annuals of Disas. Prev. Res. Inst., Kyoto Univ., No. 49 C, 2006

Complex Fluid-Sediment Interactions in Fluvial and Coastal Environments –Part 3

Hajime NAKAGAWA, Hideo SEKIGUCHI, Toyoaki, SAWADA, Taiichi HAYASHI,
Takao YAMASHITA, Tetsuo UENO, Yasunori MUTO,
Yasuyuki BABA and Shigeatsu SERIZAWA

Synopsis

This manuscript describes some of the recent research results obtained under the 21st COE project on long-term observation of sediment yields in the mountain regions, development of numerical simulation model on riverbed evolution, characteristics of flood plains and its formation by the flood, and fluvial sedimentary features in flood-stricken areas. Moreover, temporal variation of observed longshore current velocity and the relationship between the current velocity and external forces (winds and waves) is discussed, especially under storm conditions. And also, effects of Kuroshio warm current sea surface temperature on coastal wind and precipitation fields are simulated by meso-scale meteorological model MM5.

Keywords: sediment transport system, sediment yield, landslide, flood plains in valley, channel variation, geomorphological classification map, local scour, longshore current, Kuroshio, MM5

1. Introduction

This paper is a sequel to the previous contribution (Sekiguchi et al., 2004, 2005) from the Research Center for Disaster Environment and represents an outcome obtained through Research Project 3: "Atmosphere-Hydrosphere Modeling for Water/Mass Movement in River Basins and Community-based Hazard Mapping" that has been progressing in the framework of the 21st Century DPRI-COE Program, Kyoto University.

This manuscript describes some of the recent research results done at the attached observatories and laboratories or actual disaster fields on sediment yields in the mountain regions, riverbed evolution, characteristics of flood plains and its formation, and fluvial sedimentary features in flood-stricken areas. Moreover, temporal variation of observed longshore current velocity and the relationship between the current velocity and external forces (winds and waves) is discussed, especially under storm conditions. And also, the effects of Kuroshio warm current sea surface temperature on coastal wind and precipitation fields are simulated by meso-scale meteorological model MM5.In this paper, some of the recent developments are shown in modeling fluid-sediment interactions that may characterize sediment routine systems.

2. Sediment Yield

2.1 Long-term observations of sediment yield

Sediment yield in the valley influences the river environment in various forms such as turbidity and sediment movement in the watershed. It is very important in long-term valley sediment management to clarify the realities of such sediment yield in the watershed in the time series. Sediment yield is characterized by many regional factors such as geology, geomorphology, climate and vegetation. Sawada (2006; unpublished report) established a pilot study area, named Fukatani station, in the west flank of Mt.Yake in 1985 and has taken observations up to now. The test bare slope is 3 m by 10 m in plan and is underlain by

Yakedake pyroclastic-flow deposits. The amount of the sediment liberation was measured on a weekly basis by weighing the sediment that trapped sediment in test site. The specific sediment yield in the Fukatani test site is plotted in Fig.1 on a yearly basis from 1985 to 2005, together with the measured evolution of precipitation. It is seen that the specific sediment yield was highest in 1988 and then exhibited much smaller rates, even though the area had significantly high precipitations in the years 1989, 1995 and 2004.

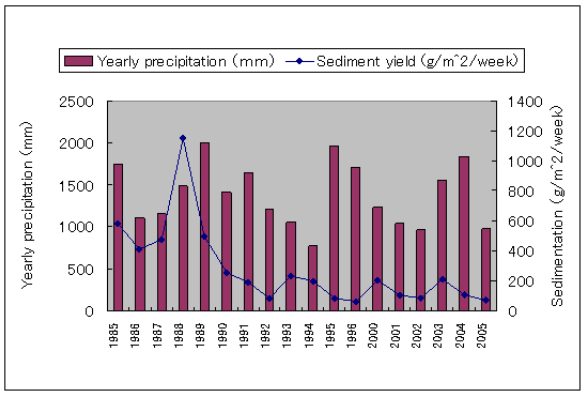

Fig.1 Measured evolution of specific sediment yield in Fukatani test site (Sawada,2006,unpublished report)

The observed result clearly indicates that the yearly rate of sediment yield from a bare slope is not a function of the annual precipitation alone.

The sampled particle size is lager in the frost heaving and thawing season than that in the rainy season. The reason for this tendency is probably because large sediment particles when dislodged can hardly be stopped in the process of downhill motion. The variation of sediment yield and rainfall with time shown in Fig.2 reveals some hysteretic characteristics. In this figure, the overall trend indicates that the sediment yield gradually

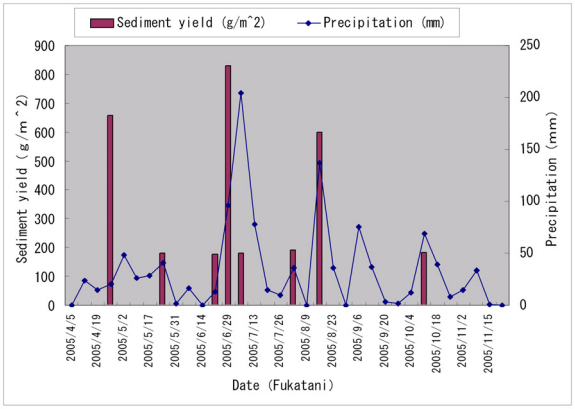

Fig.2 Hysteretic characteristics of the rate of sediment yield and precipitation

decreases from May with some sporadic increases in response to rainfalls. This trend shows annual periodicity.

The hysteretic change of the particle size distribution of sediment yield in Fukatani station is show in Fig.3. The particle size distribution shows the hysteretic change of with respect to the precipitation. Sediment yields obtained on June 21 and June 29 were low having small particle size although the rainfalls were heavy. This seems to indicate that either a thin over land flow during rainfall which can wash out fine-grained components on a steep slope or the repulsion due to raindrop occurred. The observed result show a hysteretic and seasonal characteristics of the sediment yield.

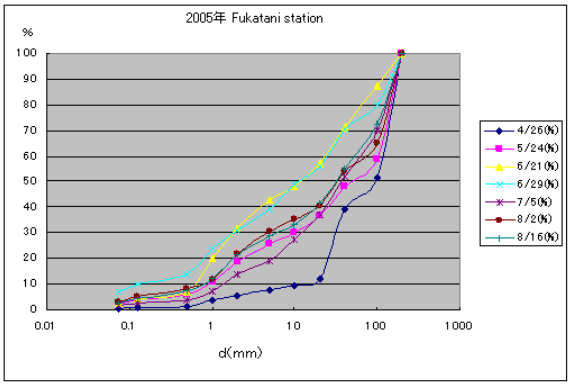

Fig.3 Hysteretic change of the particle size distribution of sediment yield in Fukatani station

2.2 Laboratory experiments on moisture content variation and landslide

Landslide is a disastrous sediment yield phenomena and also it constitutes a major threat to both lives and properties in hilly regions of the world, which experience intense rainfall events. Rain induced landslides are causing increasing damages associated with urban development and global warming. As landslide may occur in a matter of seconds without warning during a prolonged heavy rain, it is taken as one of the most destructive natural hazards.

Rain induced landslides are caused by a reduction of confining stress that holds them, as a result of pore-water pressure rise, during or following the periods of intense rain. Due to the intense rainfall, water infiltrates to the ground reducing the matric suction. As the wetting front reaches the base where the hydraulic conductivity of the underlying layer is quite low, water table starts to rise up increasing pore water pressure which possibly lead to landslide, otherwise stable slopes.

To save the life and property from the risk of the

slope failure, some sorts of prediction, which can quantitatively assign the risk to particular location and time, is essential. Numerical simulation is such a tool, which can analyze the probability of slope failure with different scenarios of rainfall and any complex soil domain.

But the current understanding of the mechanisms and conditions leading to rain induced failure is not sufficient to develop an efficient warning system (Ornse et.al., 2004). To establish the accurate warning systems, efforts have been focused on understanding the mechanism and conditions leading to these failures and on formulating procedures to predict their occurrences.

Sharma et al. (2006) investigated the difference in mechanism of moisture content variation and landslide due to rainfall, on single layer and multiple layered soil domains. In their studies, experiments on a sloped flume were done and its result of moisture movement pattern and landslides were compared with the results of numerical simulation.

(1) Infiltration

Infiltration due to transient rainfall involves moisture movement through unsaturated / saturated zones. Modeling of such flow can be done using Richards equation. Richard's equation can be written as Iverson R. M. (2000) and Sharma et al. (2005).

$$C\frac{\partial h}{\partial t}=\frac{\partial}{\partial x}\left\{K_x(h)\left(\frac{\partial h}{\partial x}-\sin\alpha\right)\right\}+\frac{\partial}{\partial y}\left\{K_y(h)\frac{\partial h}{\partial y}\right\}+\frac{\partial}{\partial z}\left\{K_z(h)\left(\frac{\partial h}{\partial z}-\cos\alpha\right)\right\} \quad (1)$$

where, h is pressure head, C is rate of change in moisture content per unit change in pressure head ($\partial\theta/\partial h$), θ is soil volumetric water content, t is time, α is slope angle, $K_x(h)$, $K_y(h)$ and $K_z(h)$ are hydraulic conductivity in x, y and z directions (Fig.1), respectively. The hydraulic conductivities may vary owing to variations of h at the unsaturated state. At saturation they becomes saturated hydraulic conductivity K_s

In order to solve RE, the constitutive equations, which relate the pressure head to the moisture content and the relative hydraulic conductivity, are required. In this study, following constitutive relationships (Equations 2 to 4) proposed by van Genuchten are used for establishing relationship of $K-h$ and $\theta-h$, with $m=1-(1/n)$.

$$K=\begin{cases}K_s S_e^{0.5}\left[1-(1-S_e^{1/m})^m\right]^2 & \text{for } h<0\\ K_s & \text{for } h\geq 0\end{cases} \quad (2)$$

$$S_e=\begin{cases}\left(1+|\beta h|^n\right)^{-m} & \text{for } h<0\\ 1 & \text{for } h\geq 0\end{cases} \quad (3)$$

$$S_e=\frac{\theta-\theta_r}{\theta_s-\theta_r} \quad (4)$$

where, K_s is the saturated hydraulic conductivity, β and n are parameters related with matric potential of soil and are measure of capillary fringe thickness and pore size distribution of soil respectively, S_e is the effective saturation θ_s and θ_r are saturated and residual moisture content respectively.

In this study van-Genuhten parameters of soil water retention curve was determined from experiment. Some of the parameters of the sediment used in the study are given Table 1.

Table 1 Parameters of the sediments considered

Sediment type	S7	S8
Saturated moisture content, θ_{sat} (-)	0.528	0.467
Residual moisture content, θ_{res} (-)	0.100	0.139
α	0.943	1.149
η	1.500	1.142
Saturated hydraulic conductivity, K_{sat} (mm/hr)	315	56
Specific gravity, Gs	2.63	2.63
Mean grain size, D_{50} (mm)	0.13	0.05
Angle of repose, ϕ (degree)	34	34

(2) Slope stability

An infinite slope theory was used for slope stability calculation. Safety factor (SF) is calculated for each grid with respect to resisting and driving shear stresses. Considering the two layers of soil over an impervious bed SF in each layer is calculated as a ratio of the resisting and driving shear stress developed at bottom of considered layer. The acting shear stress, τ_A and the resistance shear stress, τ_{AL}, at the interface of A/B-layer, are expressed respectively by

$$\tau_A=g\sin\alpha\cos\alpha\left[\begin{array}{l}D_A(1-\lambda_A)\sigma_A+\\ \rho\left\{\int_0^{D_A-H_A}\theta dz+H_A\lambda_A+H_s\right\}\end{array}\right] \quad (5)$$

$$\tau_{AL}=g\cos^2\alpha\left[\begin{array}{l}(D_A-H_A)(1-\lambda_A)\sigma_A\\ +\rho\int_0^{D_A-H_A}\theta dz\\ +H_A(1-\lambda_A)(\sigma_A-\rho)\\ +\rho H_s\end{array}\right]\tan\phi_A+c_A \quad (6)$$

where, A denotes the upper layer and B denotes the lower

layer of soil domain.

In the same manner the acting shear stress, τ_B and the resistance shear stress, τ_{BL}, at the interface of B/C-layer, are expressed respectively by

$$\tau_B = g \sin\alpha \cos\alpha \left[D_B(1-\lambda_B)\sigma_B + \rho \left\{ \int_{D_A}^{D_A+D_B-H_B} \theta dz + H_B\lambda_B + H_s \right\} \right] \quad (7)$$

$$\tau_{BL} = \left[\tau_A \tan\phi_B / \tan\alpha + g\cos^2\alpha \left\{ \begin{array}{l} (D_B - H_B)(1-\lambda_B)\sigma_B \\ + \rho \int_{D_A}^{D_A+D_B-H_B} \theta dz \\ + H_B(1-\lambda_B)(\sigma_B - \rho) \end{array} \right\} \right] \tan\phi_B + c_B \quad (8)$$

where, D and H are thickness and seepage flow depth on soil layers and H_s is surface flow depth. Similarly $\lambda, \sigma, \rho, \phi$ and c are porosity of a soil layer, density of a sediment particle, density of water, angle of repose and cohesion respectively. g is acceleration due to gravity. Subscripts A or B denotes a value in A layer or B layer. When, $H_A \geq D_A$, it is set that $H_A = D_A$ and when $H_B \geq D$, the following equation is used instead of Eq.(8).

$$\tau_{BL} = (\tau_{AL} - c_A)\tan\phi_B / \tan\phi_A + g\cos^2\alpha D_B(1-\lambda_B)(\sigma_B - \rho)\tan\phi_B + c_B \quad (9)$$

The safety factor SF_A and SF_B for A and B layer respectively are function of time dependent parameters H_A, H_B and H_s. SF for each layer is calculated using following equation;

$$SF_A = \tau_{AL} / \tau_A$$
$$SF_B = \tau_{BL} / \tau_B \quad (10)$$

The area having *SF* less then 1 is assumed to have landslide (Sharma et al., 2005).

(3) Results and discussion

The slope in two layered sediment model had the slope angle of 30°. Lower layer 10cm depth was S8 while upper 10 cm was S7 sand. All WCRs (water content reflectometer) were placed in different position (Fig.4) so that the moisture movement pattern in upper layer and lower layer both could be captured. The rainfall was supplied with the intensity of around 150 mm/hr. Throughout the experiment moisture content of the soil slope increased slowly with time towards a saturated value in response to increase in wetting front of rainwater and increasing groundwater level.

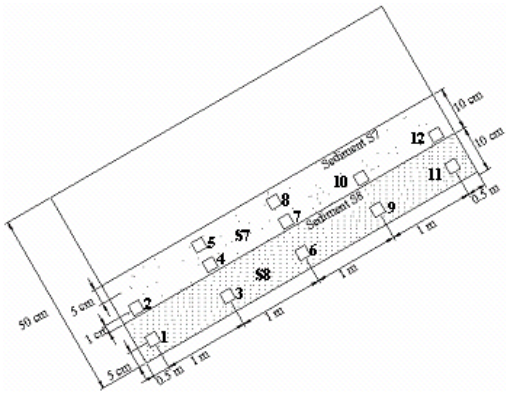

Fig.4 Arrangement of WCRs (1-12) (upper layer S7 sand and lower layer S8 sand)

Fig.5 shows the numerical and experimental simulation of the temporal water content profile and the timing of landslide. In this case the failure on the upper layer consisting of S7 occurs first. The numerical and simulated moisture content profile are very close to each other for all WCRs. Simulated and experimental failure time are also quite close to each other. Complete slide can also be dictated from Fig.5 at the WCR-4 and WCR-7, which were due to the exposure of WCR probes to air after movement of whole soil mass surrounding them. But the actual failure i.e. start of tilt occurs some

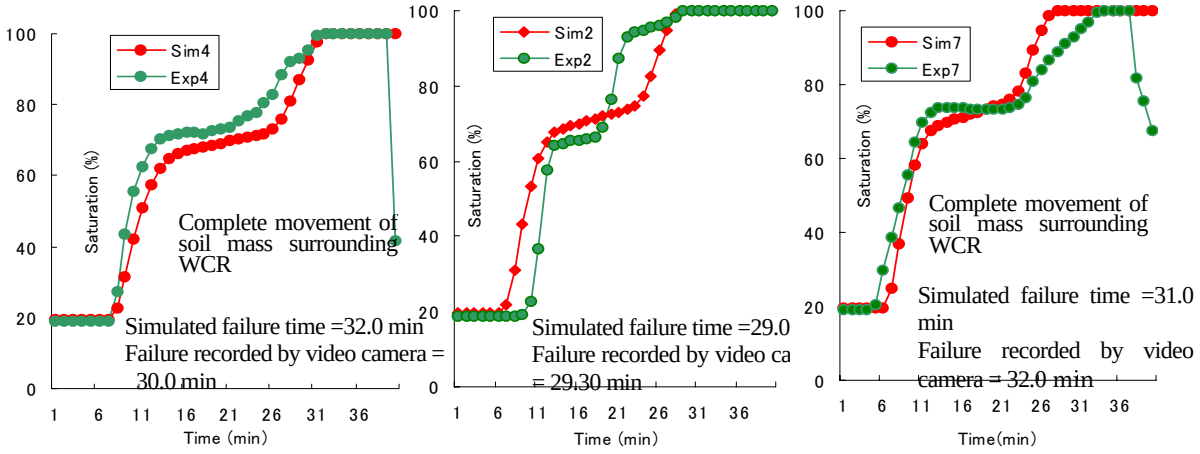

Fig.5 Experimental and simulated results of the water content profile and landslide time (WCR-4, 2and 7)

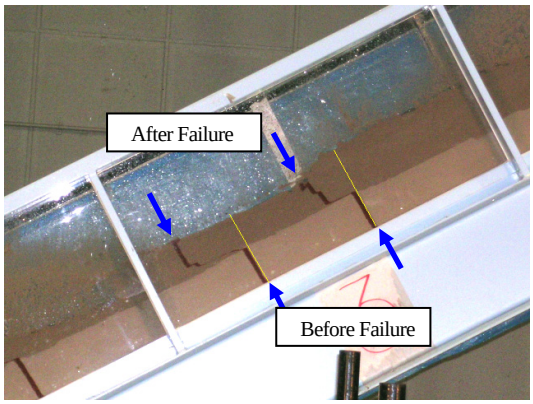

Fig.6 Failure of the upper layer. Yellow lines show original positions of red strips (initially 2.33m and 2.66m from downstream end)

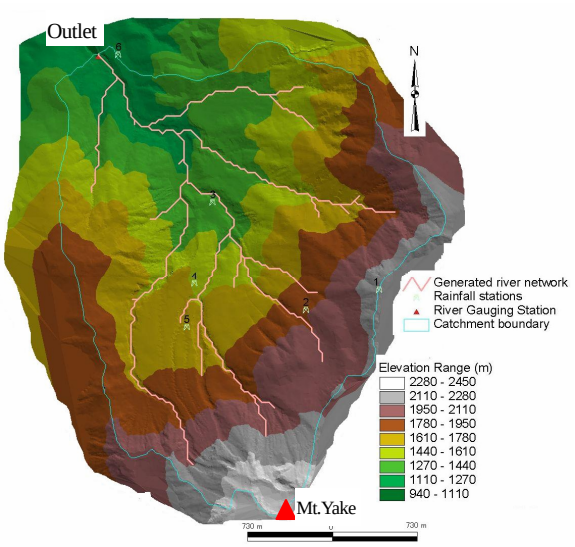

Fig.7 Elevation and channel network in the Ashiarai dani basin

minutes before the complete collapse which was captured by video camera. Overlaying the initial state of the sand strips on final stage at different time steps helped to find the start of the tilt of red sand strips.

From Fig.6 it is obvious that the failure depth is just 10 cm in this case. Only top 10 cm of S7 sediment, which has high hydraulic conductivity, slides and bottom 10cm of S8 sediment remains in its original position.

In the experiment of the two-layered slope, only the top layer of sand with 10cm depth slides. Due to the smaller hydraulic conductivity of the under laying sand, water table rises up from the bottom of upper layer which causes failure of the upper layer only. It helps to conclude that depth of failure depends highly on the layering characteristics of the soil domain in the field. The results of numerical simulation and laboratory experiments of temporal changes in moisture movement and landslide are quite comparable. It shows the potential of the numerical model to be extended for the use in real field.

2.3 Application to the Ashiarai dani basin

Observational studies have been made on the rainfall and sediment runoff processes in the Ahiarai dani basin whose catchment area is about 6.5 km^2, a tributary of the Gamata River in the northern Japan Alps. In this area, where sediment yield is extremely high, the movement of debris takes a variety of forms, such as landslide, debris flow and general bed load, which makes the area suitable for an experimentally basin in the research on sediment routine systems.

By coupling a subsurface flow model used in the landslide prediction with an overland flow model, rainfall runoff calculation was executed for the Ashiarai dani basin. Fig.7 is an elevation map of the basin and a channel network and rain gauge stations are shown on the map. The elevation of the basin is in the range of around 940 - 2450 m.

In the calculation, distributed rainfall is used for the basin which is divided into several theissien's areas considering the rain gauge stations. Slopes are assumed to have two layers, i.e., upper layer of 0.5 m deep and lower layer of 3.5 m deep, respectively. It is also supposed that the initial water table height is 0.5 m at bottom of the lower layer.

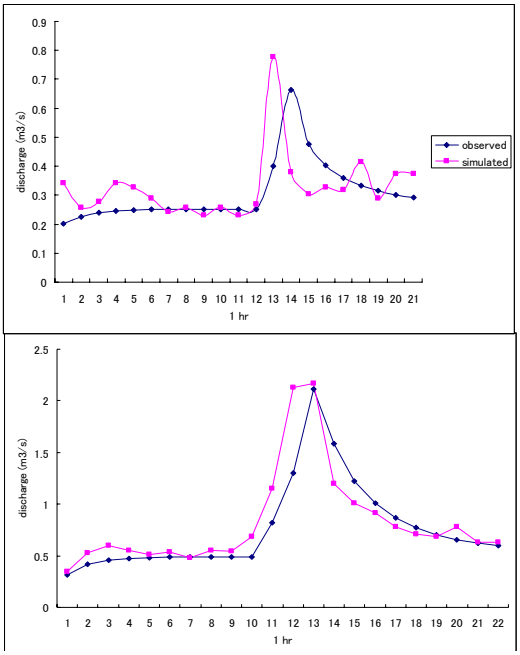

Fig.8 Comparisons of observed and calculated flood discharge (without sediment)

Fig.8 shows the comparisons of the calculated and observed water discharge hydrographs in case that the flow contains no sediments. The several parameters such as water conductivity and initial height of water table were tuned up appropriately in the calculation. From the figure, it is found that the model can reproduce the observed water discharge well.

Because we have never observed heavy rainfalls which generate catastrophic landslide disasters in the basin, the imaginary heavy rainfall was adopted to simulate the occurrence of landslides and a following debris flow phenomena. Fig.9 shows sediment discharges in case that 0%, 10%, and 20% landslide mass reaches the channel. In the calculation, the landslide mass is given within a short period of 10 seconds with volumetric sediment concentration of 50% at the nearest channel section from the landslide site as an input boundary condition of the landslide mass into the channel. The very sharp peek discharge of flow is formed in case of 20% and this flow is so called a debris flow. Such simulation must be useful to make a sediment hazard map in the basin.

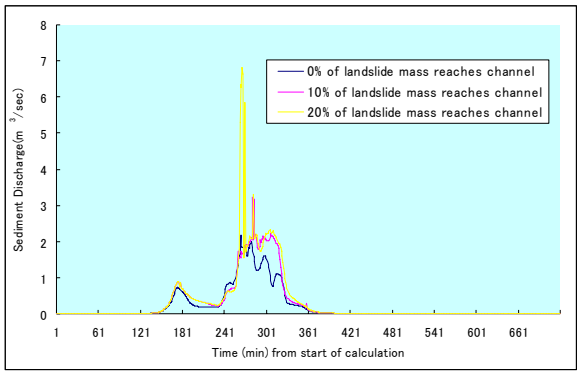

Fig.9 Sediment discharges in case that 0%, 10%, and 20% landslide mass reaches the channel.

3. The Flood Disaster and Configurations of Flood Plains in Mountainous River

Severe flood disasters due to heavy rainfalls occurred in the Yosasa River basin in 1998 and in the Asuwa River basin in 2004. The flood disasters in the mountainous area are discussed on the basis of the field survey and aerial photographs taken after the flood. It was cleared that the damage due to flooding was related to the configuration of flood plains in valley. The characteristics of flood plains and its formation in the case where the configuration of flood plains had a positive effect on the damage due to flooding are investigated.

3.1 The flood disaster and the configuration of flood plains in the Yosasa River basin

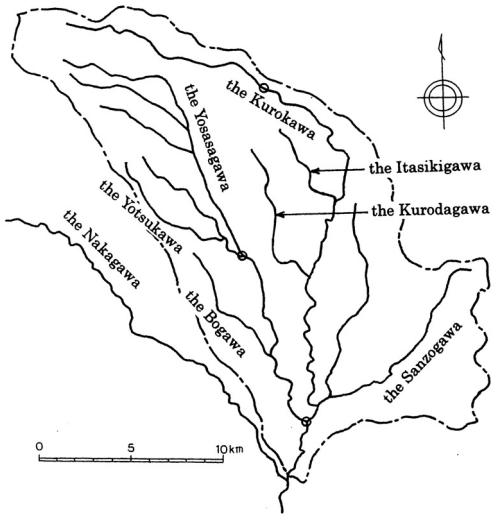

Fig.10 The map of the Yosasa River basin

The flood discharge was about four times as large as the average conveyance of the river channel in the research section. The map of the Yosasa River basin is shown in Fig.10. In this figure, white circles are drawn on both ends of the research section. The research section is 13 km from the junction between the Yosasa River and the Kurokawa River in the Yosasa River and 29 km from the junction in the Kurokawa River. The catchment area of the Yosasa River is 127 km^2 and that of the Kurokawa River is 98 km^2. The daily rainfall at Nasu observatory reached 640 mm.

The many new channels were formed in the place where curved river channels were narrow (Ueno, 2005). However, in the 1.2～9.7 km section of the Kurokawa River, new channel was not formed and the damage due to flooding was slight. As an example, the aerial photograph taken after the flood in 3.8～5.8 km section of the Kurokawa River is shown in Fig.11. In this photograph, the lowland belt exists along inner side in

Fig.11 The aerial photograph taken after the flood in 3.8～5.8 km section of the Kurokawa River

the river bend. The damage due to flooding in this section was slight because the flood flowed over the lowland belt.

The variations of bed slope of the Yosasa River and the Kurokawa River are shown in Fig.12. It is noticed that the bed slope in the 2～8 km section of the Kurokawa River is larger than that in the 10～19 km section. Sediment is deposited in the 10～19 km section of small bed slope. Therefore, in the 2～8 km section, sediment discharge is small and the river channel is eroded. Floods eroded outer side in the river bend and river bed, and the bend section moved to downstream and lateral direction. Consequently, the lowland belt was formed along inner side in the river bend.

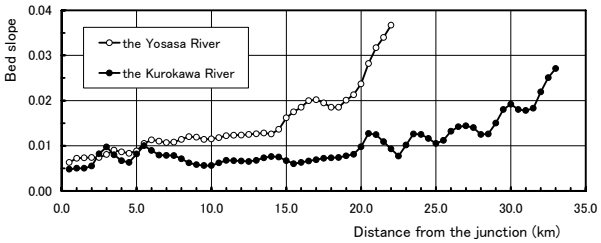

Fig.12 Variations of the bed slope of the Yosasa River and the Kurokawa River

3.2 The flood disaster and the configuration of flood plains in the Asuwa River basin

Severe flood disaster due to heavy rainfall occurred in the Asuwa River basin on July 18, 2004. The flood discharge was much more than the average conveyance of the river channel in the research section. The map of the Asuwa River basin is shown in Fig.13. In this figure, white circles are drawn on both ends of the research section. The research section is 13～36 km from the

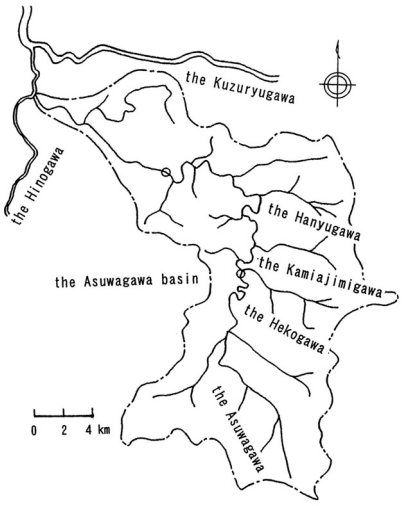

Fig.13 The map of the Asuwa River basin

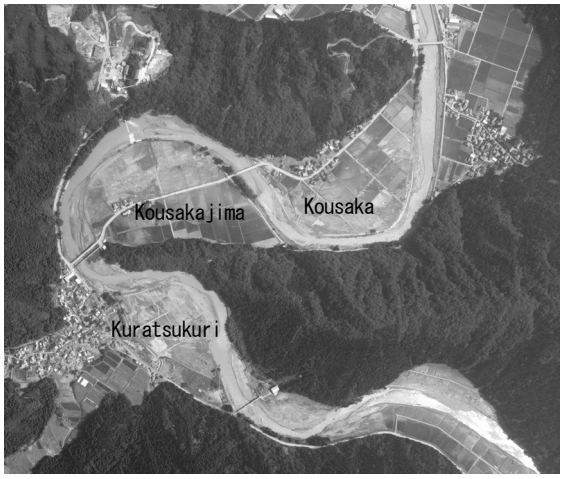

Fig.14 The aerial photograph taken after the flood in 26.4～30.4 km section of the Asuwa River

downstream end of the Asuwa River. The catchment area of the Asuwa River is 415.6 km^2. The rainfall in 6 hours at Miyama observatory reached 229 mm.

The characteristic configuration of flood plains is seen in upstream area of the junction (26 km point) between the Asuwa River and the Hanyu River. As an example, the aerial photograph taken after the flood in 26.4～30.4 km section of the Asuwa River is shown in Fig.14. The shape of flood plain surrounded by river channel and mountain area is nearly triangle. In the area of Kuratukuri, Kousakajima and Kousaka, the vertical drop from upstream part of the flood plain to river bed is smaller than that from downstream part of the flood plain to river bed. It is inferred that enormous floods flowed all over the flood plain and formed sand bars there in the far past, and the sand bars did not move for repetition of enormous floods because the sinuosity of the valley is larger (Kinoshita and Miwa, 1974). Usual floods flowed through the lower part near the front of sand bars and the present river was formed. This is the way that the characteristic configuration of flood plains was formed. The severe damage in these flood plains was limited to the upstream part of flood plains because the slope of flood plains is smaller than that of river bed.

The variations of the bed slope of the Asuwa River and valley width are shown in Fig.15. It is noticed that the bed slope in the 26～40 km section is larger than that in the 41～44 km section. Sediment is deposited in the 41～44 km section where the bed slope is small. Therefore, in the 26～40 km section, sediment discharge is small. On the other hand, as shown in Fig.13, the Heko River and the Kamiajimi River join the Asuwa River in the upstream research section (26～36 km section) of the

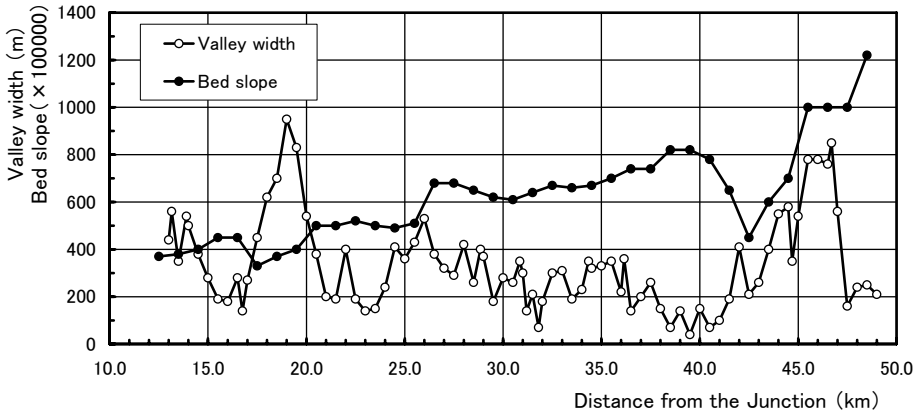

Fig.15 Variations of the bed slope of the Asuwa River and valley width

junction between the Asuwa River and the Hanyu River. These rivers supply almost constant sediment to the Asuwa River. In 26～36 km section, the bed slope (0.007) and the valley width (300m) are roughly constant. Under such conditions, the characteristic configuration of flood plains was formed.

4. Studies of Fluvial Sedimentary Features in Flood-Stricken Areas

4.1 Introductory remarks

Most of the alluvial plains in Japan are products of flood-related sedimentation. The evidences include geomorphological features, such as perched rivers, natural levees and crevasse splays. Indeed, geomorphological classification maps of flood-stricken areas have been recognized as one of the most systematic and useful representations for flood-plain management (e.g., Oya *et al*., 1998). It is important herein to point out that many of such classification maps were produced a few decades ago in print version, thereby overlooking a range of significant land-use evolution we now experience.

Furthermore, such a classification map merits further flexible descriptions for flood-hazard management. Two illustrative situations are given in Fig.16 to emphasize such societal needs. Refer to Fig.16(A). The question may then arise as to what sort of engineering measures were done in the sections where the current levees cross the former river channels. In view of Fig.16(B) one may pose a question why the old river channel is isolated from the current river course.

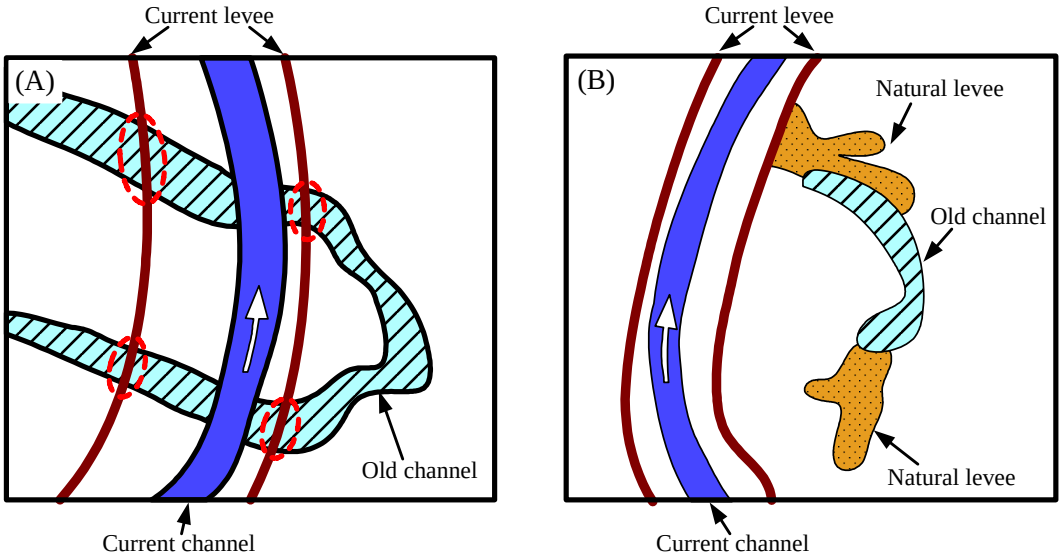

(A) Levee sections built across former river channels (B) An isolated section of former river channel

Fig.16 Examples of geomorphological features that merit further information

The following outlines a recent levee-breaching case, with the aim of demonstrating the capability of high-resolution digital representation for future flood-plain management.

4.2 Crevasse-splay sedimentary features – A case study

This sub-section outlines a case study of the 2004 levee breaching case with the Maruyama River (Azuma et al., 2006). Typhoon 0423 made landfall in Osaka at 18:00 on 20 October 2004 and brought about precipitation as much as 278mm in the Toyooka area over a two-day period (20-21 October 2004).

According to testimony of residents, the overflow occurred at Tachino around 21:00 on 20 October 2004 on the right bank of the Maruyama River. Approximately two hours later, the right bank breached, bringing about serious damage to the adjacent buildings, facilities and paddy field (refer to Fig.17).

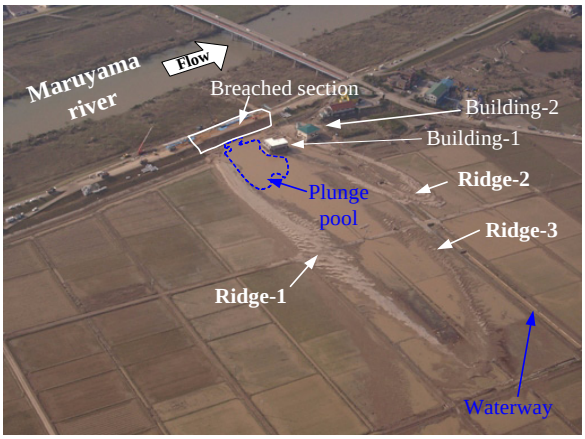

Fig.17 Aerial photograph of the flood plain, taken on October 25, 2004 (courtesy of Prof. Y. Fujita)

The breaching-induced topographical changes were measured using the method of digital photo-theodolite surveying and are summarized in the form of Fig.18 (Azuma et al., 2006). Note in this figure that the relative heights of a total of 1,029 survey points are plotted in terms of contours, together with the spatial information from Digital Map 2500 of KINKI which is issued by the Geographical Survey Institute (SGI). Ridge 1 extended 300 meters in a direction nearly normal to the levee. The height of the ridge took a maximum value (2.2m) near the levee and decreased gradually with distance from the levee. The occurrence of ridge 2 is also apparent in Fig.18. Although ridge 3 manifests itself as a relatively narrow strip of sediment in Fig.17, it is only marginally discernible in Fig.18. This performance suggests that ridge 3 was a less pronounced feature and was likely to have undergone secondary modifications.

The results of the breaching-related volume analysis are as follows (Azuma et al., 2006). The volume of sediment by erosion is equal to 21,000m^3 which is the sum of the 16,000m^3 from the breached levee and the 5,000m^3 from the plunge pool. The volume of deposition is equal to 17,000m^3 which is the sum of the 12,000m^3 from ridge 1 and the 5,000m^3 from ridge 2. It is thus

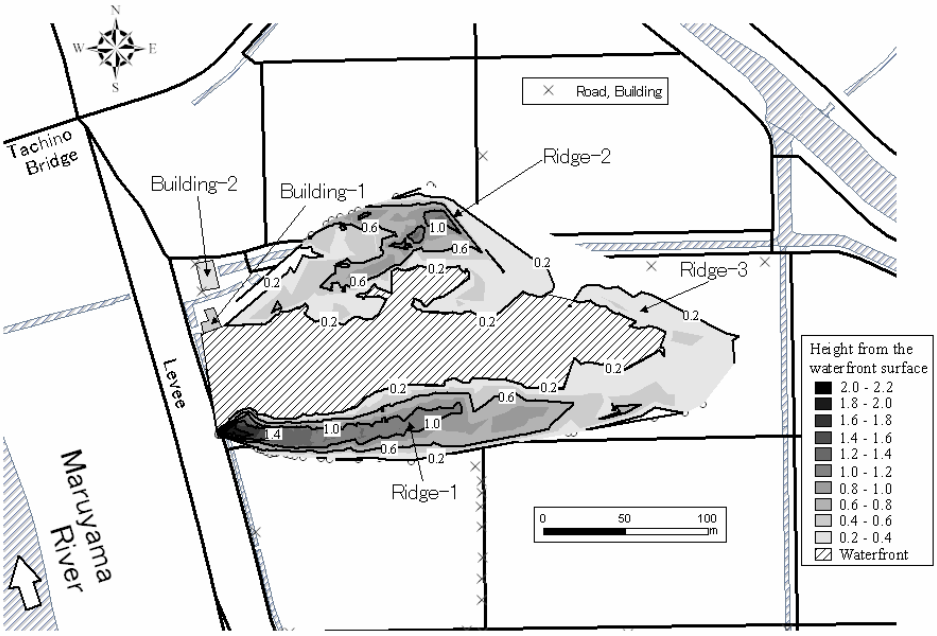

Fig.18 Breaching-induced topographical changes in flood plain (Azuma et al., 2006)

concluded that the sediment yield due to the breaching largely resulted in the formation of ridges 1 and 2.

4.3 High-resolution digital geomorphological mapping

The 1977 GSI-issued classification map of the flood-stricken Maruyama River basin has recently been reprinted, without any updating. A part of it is reproduced in Fig.19(A). Although the classification map is informative and useful in its own right, there are limitations in description. For instance, it does not represent the land-use evolution that has occurred over the past thirty years or so.

In fact, one may notice a few buildings standing on a part of the former meandering course of the Maruyama River (see Fig.19(B)). Note that this figure was constructed first by digitizing the 1977 version of the classification map and then by superimposing GSI's high-resolution spatial-data framework from a Digital Map 2500 (KINKI-1), together with the crevasse-splay sedimentary features measured (Azuma et al., 2006).

Interesting observations may be made by comparing Figs.19(A) and (B). For instance, the initially meandering Maruyama river course was essentially straightened, with the old-channel sections being turned into land for use. Those sections with several buildings now standing should have been carefully treated from an engineering standpoint.

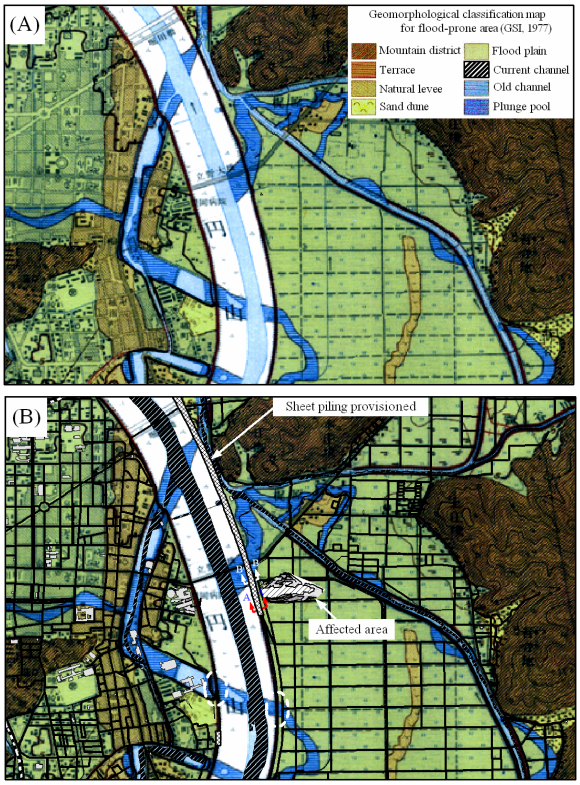

Fig.19 (A) 1977 GSI's geomorphological classification map of Maruyama River basin. (B) Extended digital representation by Azuma et al. (2006)

As far as risk management of flood-related hazards is concerned, such representation of former river channels or the like on a geomorphological classification map is just a start for thorough engineering assessment. Indeed, a range of important engineering measures should be represented as well, as illustrated in Fig.19(B). Note a long section of sheet piling on the right bank of the Maruyama River. The sheet piling was performed many years ago, prior to the 2004 flood event, so as to reinforce the seepage-vulnerable areas. Accordingly, the presence of the old river channel near Tachino should not have affected the 2004 levee-breaching case, because the foundation soil below the levee was well protected by the sheet piling work.

This statement may be supported by the observation that the foundation soil below the levee withstood the excessively high flood stage in October 2004, and that the breeching was triggered by the overflowing water (Toyooka River and National Highway Office, 2005).

4.4 Flow and local scour around a submerged spur dike

A numerical model was developed to simulate the flow and local scour around hydraulic structures (Zhang, et al., 2006). The model solves the 3D RANS (Reynolds Averaged Navier-Stokes Simulation) equations for the flow with FVM formulation on an unstructured mesh. Arbitrary polyhedral mesh can be utilized to resolve complex geometries. Local scour due to bedload transport is simulated through the sediment continuity equation and empirical formulae for sediment transport rate.

Typical spur dikes in the river engineering usually suffer from the over-topping flow during the flood season. In order to understand the flow characteristics and local scour around submerged spur dikes, Ishigaki and Baba (2004) have carried out a series of experiments in the Ujigawa Hydraulics Laboratory, DPRI, Kyoto University. In this verification, the model is tested under the same hydraulic conditions as one of their experimental cases.

The mesh system around the spur dikes used in the computation is shown in Fig.20. Fig.21 shows the comparison of the resulted bed deformation after 1 hour. In both the experiment and computation, the bed

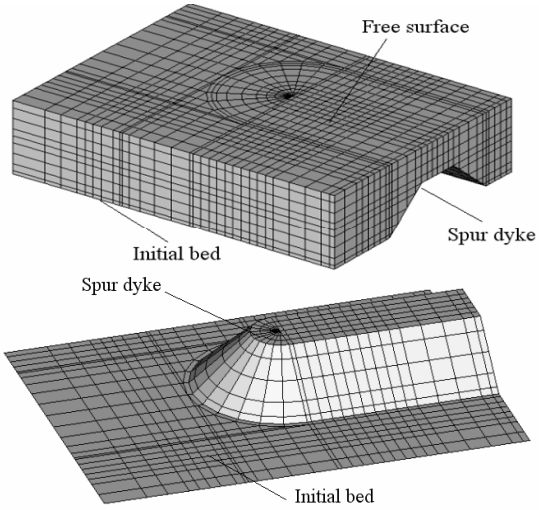

Fig.20. Unstructured mesh system around the spur dyke at initial stage (not to scale).

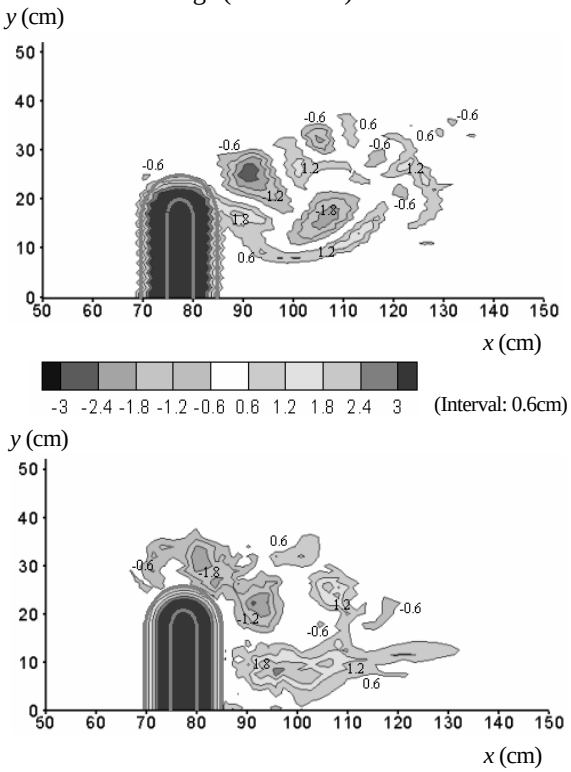

Fig.21 Bed deformation around the spur dyke after 1 hour (Experiment: Top; Computation: Bottom)

deformation is confined to the proximity of the spur dike. In general, the scour-deposition pattern shows some simplicity. There are two big obvious scour holes downstream of the spur dike. In the experiment, the scour hole depths are 2.78 cm and 2.05 cm, respectively. The corresponding results of the computation are 2.33 cm and 2.71 cm, respectively. The occurrence of two big scour holes can be interpreted as a result of both flow separation and downward overtopping flow.

The predicted local scour holes locate a little different from those of the experiment. The error may come from several sources such as equilibrium bedload transport equation used, accuracy of dike-shape reproduced by unstructured meshes, and etc.

5. Longshore Currents in Offshore Region under Storm Conditions

In this section, temporal variation of observed longshore current velocity and the relationship between the current velocity and external forces (winds and waves) is discussed, especially under storm conditions. Longshore currents are generated by wave and wind in coastal zone, and the currents associate closely with longshore sediment transport. The longshore sediment transport could be one of important factors in long-term perspective of the beach profile change because long-term profile changes is generally assumed to be related to alongshore variations in the longshore sediment transport rate.

Under storm conditions, strong longshore currents have been observed in both surf zone and offshore and these longshore currents have strong correlation with longshore component of wind speed. These wind-induced longshore currents have enough magnitude to generate considerable sediment transport in the wide area of coastal region. The existence of longshore currents under storm conditions could lead to wide-area morphological change, and it is important to demonstrate the mechanism to generate strong longshore currents under storm conditions.

5.1 Field observation under storm conditions

The joint field observation cooperated with several universities and institutes was carried out around Hazaki Oceanographical Research Station (HORS, MLIT, Fig.22) from July to October 1999. Waves and currents

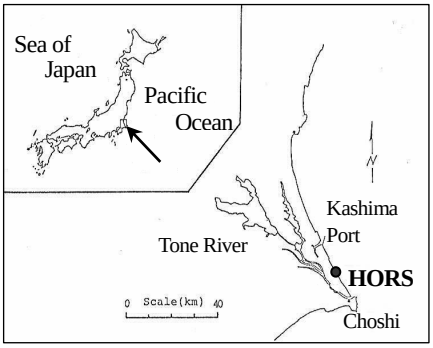

Fig.22 Hazaki Oceanographical Research Station

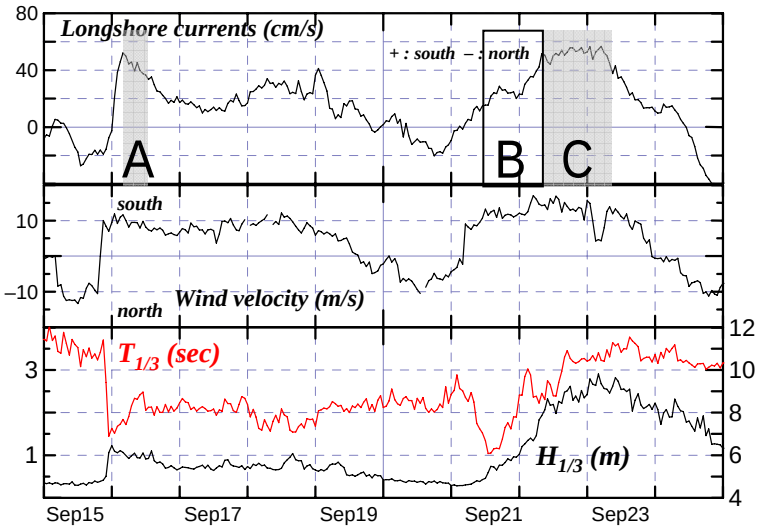

Fig.23 Temporal variations of longshore current velocity (top), longshore component of wind speed (middle) and significant wave height and period (bottom)

were measured at an offshore point (the depth is 10m deep) and high frequency ADCP (Acoustic Doppler Current Profiler) was used to investigate vertical distributions of current velocity. From observational results, it was found that strong longshore currents occur under storm conditions. These currents under storm conditions are uni-directional and have strong correlation with the longshore component of the wind speed with time lag of about 4 hours. Therefore, the longshore currents in this case have the characteristics of wind-driven currents (Baba et al. 2000).

Fig.23 shows an example of temporal variations of the depth-averaged longshore velocity, longshore component of wind speed and significant wave height ($H_{1/3}$) and period ($T_{1/3}$), where the longshore component of tidal current is eliminated from observed longshore velocity component.

Strong longshore currents (more than 40cm/s) are observed twice (A & C in Fig.24) in this period. These severe conditions causes considerable sediment transport in longshore direction and could give much influence to wide-area morphological change.

5.2 Analysis of longshore currents under storm conditions

Relationship between longshore current velocity and external forces is herein discussed using following observed results:

1) depth-averaged longshore current velocity
2) longshore wind speed at 10m above sea surface
3) significant wave height ($H_{1/3}$) and period ($T_{1/3}$)

The current velocity and wave properties were measured at same point (depth of about 10m) and wind speed at the front edge of the pier of HORS. As mentioned above, wind speed and current velocity in longshore direction have strong correlation with time lag of about 4 hours. In present analysis, the time-averaged wind speed for over the past 4 hours is employed as a representative wind speed. Wave direction was not measured in this observation.

Fig.24 shows the comparison between both drag coefficients under storm condition (wind speed is more than 10m/s). Drag coefficients using observed wind speed data are derived by the equation developed by WANDI group (1988), and drag coefficients using observed current velocity data by sea-surface stress balance concept with the bulk formulae of the shear stresses (employing the quadratic laws).

When the currents developed more than 40cm/s (in Sep 22), drag coefficients derived from current velocity exceed the ones referenced to the wind speed. This result means that the assumption of wind-referenced drag

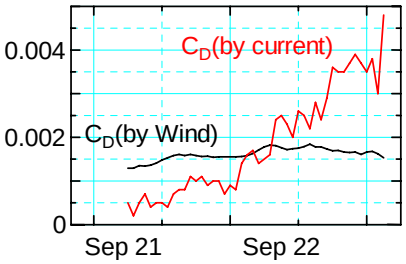

Fig.24 Comparison between drag coefficients under storm condition (BLACK: referenced by wind velocity, RED: estimated by balance equation of surface stress)

coefficient in the bulk formulae is not enough to express well-developed current condition and additional parameter is required in order to demonstrate temporal variation of observed current velocity.

Fig. 25 illustrates the temporal variations of wave steepness (H/L), wave age (C/W) and dimensionless wave energy (E*) under well-developed current condition. In the early stage of storm condition (the latter half of Sep 21), wave energy increases steadily. When wave energy reaches almost constant value ($E^* \approx 10^3$), wave steepness becomes large number ($H/L \approx 0.025$). This period with stable wave energy and large wave steepness corresponds approximately to the period of well-developed current condition. Thus, large wave steepness has some relation with the development of current velocity, and it is expected that some part of wave energy transforms from wave to mean flow through wave dissipation and that enhanced surface stress leads to the generation of strong longshore currents.

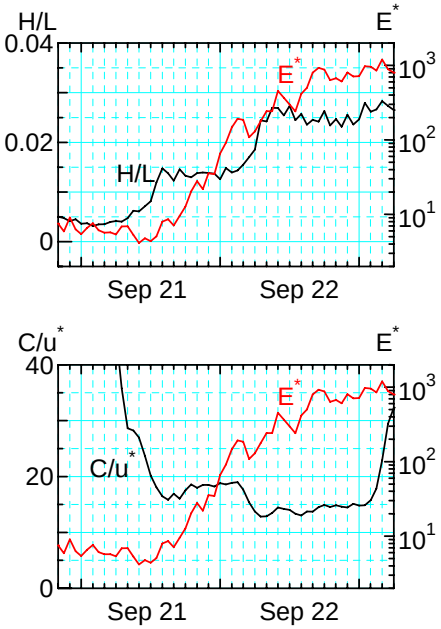

Fig.25 Temporal variations of wave steepness (H/L), wave age (C/W) under storm condition and dimensionless wave energy E* ($E^* = H^2 T_{1/3}^4/g^2$, where E=wave energy; $T_{1/3}$ = significant wave period)

The relation between dimensionless wave energy (E*) and dimensionless roughness on the sea surface referenced by current velocity illustrates in Fig.26. The square of E* is one of parameters related to wave energy dissipation. In period B & C in Fig.23, the dimensionless roughness increases according with the growth of the square of dimensionless wave energy and seems to converge with a value determined by wind and wave conditions. This result means that the development of wave condition has considerable contribution to the generation of well-developed current condition.

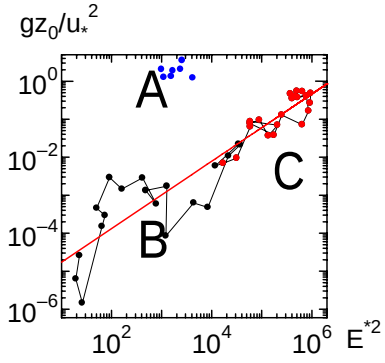

Fig.26 Dimensionless wave energy E* vs dimensionless roughness on sea surface (u*:shear velocity, z_0:roughness height)

6. Effects of Kuroshio Warm Current SST on Coastal Wind and Precipitation Fields Simulated by Meso-scale Meteorological Model MM5

6.1 Introductory remarks

The latent heat flux at the sea surface has a big influence on atmospheric structure or movement, and the quantity of atmospheric motion and heat exchange at the sea interface are processes governing the coastal climate, such as temperature, winds and rainfall in the fluvial land and connecting coasts. It is expected that winds and precipitation in coastal area of Japan facing the Pacific Ocean are strongly affected by the Kuroshio Warm Currents (KWC). The huge quantity of heat and vapour supplied from KWC cannot be disregarded in meteorological prediction which results in the evaluation accuracy of wind waves, currents and river discharges through the watershed connecting to coastal ocean.

Even from the viewpoint of Coastal Engineering, prediction of rainfall and runoff is one of most important tasks because rainfall makes the basis of a water cycle and transport of sediment and nutrient to coastal ocean through surface and interflow runoff, ground water flow and rivers.

In this study, numerical experiments were conducted to simulate the impact of the spatial distribution of ocean heat capacity on the atmospheric environment in the coastal regions. The effects of ocean surface temperature distribution on the characteristics of

rainfall and surface wind fields were also examined in the numerical experiments.

The meso-scale meteorological model, NCAR/PSU MM5 was employed for weather simulation. Two kinds of sea surface temperature (SST) data in the lowest atmospheric boundary were examined. Those are the skin temperature in Global Forecast System forecasts (GFS) by NCEP's Environmental Modeling Center, and the SST from JCOPE (Japan Coastal Ocean Predictability Experiment) by Research Center for Global Change (FRCGC) supported jointly by Japan Aerospace Exploration Agency (JAXA) and Japan Agency for Marine-Earth Science and Technology (JAMSTEC).

6.2 Numerical simulation methods

The Global Forecast System forecasts (GFS) collects observations for 2 hours and 45 minutes past synoptic time and makes a 16 day forecast from 4 synoptic times per day, namely 0000 UTC, 0600 UTC, 1200 UTC, and 1800 UTC. The GFS starts at the highest resolution (T254 L64) but drops resolution during the forecasts. After 84 hours, the GFS drops to the resolution of T170 L42.

JAMSTEC has started an ocean weather forecast experiment as a part of the JCOPE which has begun in October 1997. The present JCOPE system has achieved near operational forecast using almost all available data obtained from satellites, ARGO floats and ships. The routine prediction of oceanic variation combining with in-situ verification of the results, will significantly contribute to improve atmosphere-ocean models for prediction of longer-term climate change.

The skin temperature of Global Forecast System (GFS) has a coarse resolution therefore Kuroshio Warm Current (KWC) could not describe well in these data (see Fig.27). On the other hand, the sea surface temperature (SST) of JCOPE has a well resolution as shown in Fig.28.

NCEP/NCAR data was employed as a initial and background data for MM5 simulation. Nudging of pressure fields is conducted every 6hrs to correct the position of typhoon. Simulation period is from 00UTC 5 August 2003 to 06UTC 9 August 2003 in order to capture the main period of Typhoon 0318 effect on the Kii Peninsula r(Fig.29).

The cumulus parameterizations used in the simulation are shown in Table 2. Fig.30 shows the

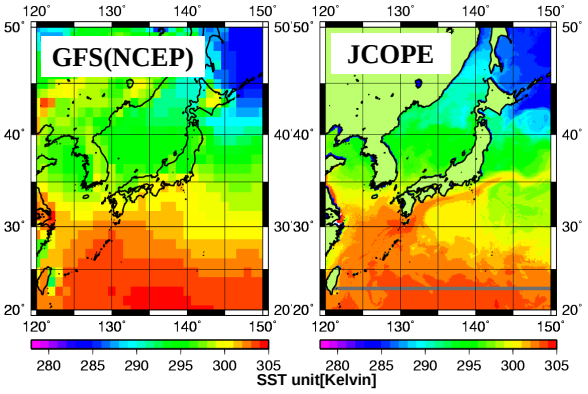

Fig.27 GFS's skin temperature Fig.28 JCOPE's SST

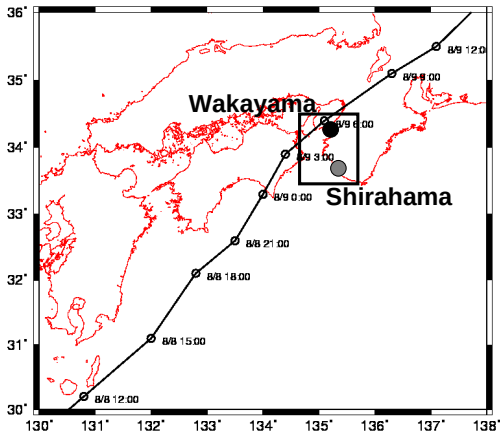

Fig.29 Typhoon track data by JMA

Table 2 Used Cumulus Parameterization

Cumulus Parameterization	Grell（No use in Domain3e）
Cloud physics process	Simple Ice
Planetary boundary layer	MRF PBL
Radiation process	Cloud-radiation scheme
Land-surface process	5-layer soil scheme

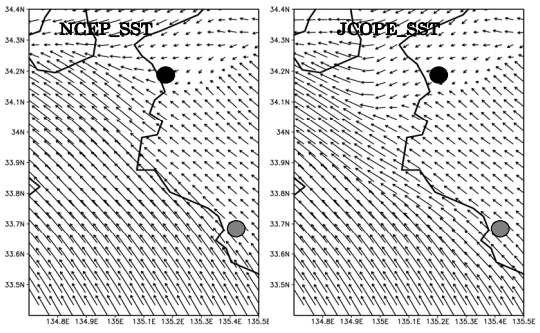

Fig.30 Wind vector fields at AUG 8 12:00UTS.（left: GSF data and right: JCOPE SST data)

comparison of wind vectors estimated by using GSF and JCOPE SST data on the west coast of the Kinki Peninsular.

Fig.31 shows the time series of precipitation

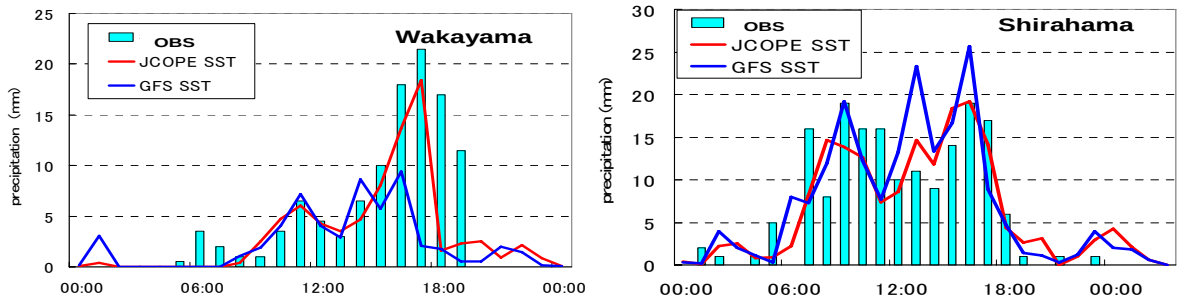

Fig.31 Precipitation observed and computed by using SSTs of GFS and JCOPE at Wakayama and Shirahama

observed and computed (two kinds of SSTs) at Wakayama and Shirahama on the west coast of the Kii Peninsular. It can be clearly observed that predicted precipitation using JCOPE SST can reproduce the observation very well, however, simulation by using GFS SST under-estimates observation at Wakayama and over-estimate at Shirahama.

Fig.32 shows the total rainfall differences estimated by using JCOPE minus GFS(NCEP). Shaded area indicates plus (JCOPE>GFS) and unit is mm. It can simulate a heavier precipitation in the area of the west coast of Kii Peninsular and north area of Osaka Bay.

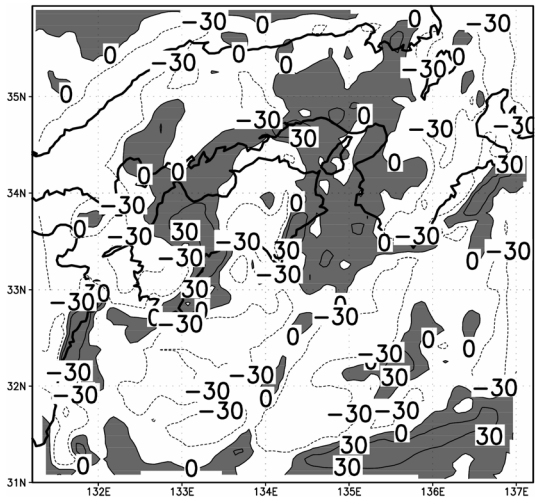

Fig.32 Total rainfall differences estimated by JCOPE minus GFS(NCEP) SST data. (unit:mm)

7. Conclusions

The results obtained in this project are summarized as follows;

The observed result on the sediment yield from the bare slope clearly indicates that the yearly rate of sediment yield is not a function of the annual precipitation alone. Moreover, rather high sediment yield in spring is due to frost heaving and freeze thaw.

A numerical model to simulate the infiltration and landslide due to rainfall was developed. The simulated results as timing of landslide and moisture movement pattern from experiment and numerical simulation are found to be quite close.

The flood disasters in the mountainous areas such as the Yosasa and the Asuwa River basins are discussed on the basis of the field survey and aerial photographs taken after the flood. It was cleared that the damage due to flooding was related to the configuration of flood plains in valley. The characteristics of flood plains and its formation in the case where the configuration of flood plains had a positive effect on the damage due to flooding are investigated.

The outlines of a recent levee-breaching case in the Maruyama River were shown with the aim of demonstrating the capability of high-resolution digital representation for future flood-plain management.

Some descriptions and applications of a 3D numerical model are shown through which the flow structure and the local scour around hydraulic structures can be simulated. The model applicability has been confirmed through reasonable predictions of the flow structure and local scour holes in a laboratory experiment.

Dimensionless roughness increases according with the growth of the square of dimensionless wave energy and seems to converge with a value determined by wind and wave conditions. This means that the development of wave condition has considerable contribution to the generation of well-developed current condition.

It was made clear that wind and rainfall prediction by MM5 can be improved by using the high resolution SST data （JCOPE data in this study） which can describe warm current distribution near the coastal region (Kuroshio Warm Current in this study).

Acknowledgements

The authors are grateful to Mr. Shida Masao, Dr. Azuma Ryokei, Dr. Zhang Hao, Mr. Sharma R.H., Mr. Yamaguchi Kosei, Mr. Kriyo Sambodho, and Mr. Ano Makoto, who helped to carry out our COE research projects.

References

Azuma, R., Sekiguchi, H. and Ono, T. (2006): Performance of levee systems at flood stage, Annuals, Disas. Prev. Res. Inst., Kyoto University, No. 49C (in print).

Baba, Y., Imamoto, H., Yamashita, T. and Kato, S. (2000): Wind-driven currents in shallow water and its wind response - Analysis of ADCP data at Hazaki Oceanographical Research Station in 1999-, Proc. 47th Coastal Eng., JSCE, 446-450 (in Japanese).

Iverson R. M. (2000): Landslide Triggering by Rain Infiltration, Water Res. Research, Vol.36(7), pp.1897-1910.

Kinoshita, R. and H. Miwa (1974): River channel formation which prevents downstream translation of transverse bars, Shin Sabo, 94, pp.12-17 (in Japanese).

Ornse, R. P., Shimoma, S., Maeda, K., and Towhata, I. (2004): Instrumented Model Slope failure due to water Seepage, J. Natural Disaster Science, Vol.26 (1), pp.15-26.

Oya, M., Maruyama, Y., Umitsu, M., Haruyama, S., Hirai, Y., Kumaki, Y., Nagasawa, R., Sugiura, M., Kubo, J. and Iwahashi, J. (1998): Guidance for reading and making the geomorphologic classification map, Kokon Shoin Publishers, Tokyo (in Japanese).

Sharma, R. H. and Nakagawa, H. (2005): Predicting timing and location of rainfall triggering shallow landslides, *Annual J. of Hydraulic Engineering*, JSCE, Vol. 49, pp.43-48.

Sharma, R.H., Nakagawa, H., Baba, Y., Muto, Y. and Ano, M. (2006): Laboratory experiments on moisture content variation and landslide caused by transient rainfall, Annual Journal of Hydraulic Engineering, JSCE, Vol.50, CD-ROM.

Sharma, R.H., Nakagawa, H., Baba, Y., Muto, Y. and Ano, M. (2006): Laboratory experiments on moisture cont

The WANDI Group. (1988): The WAM Model – A Third Generation Ocean Wave Prediction Model, J. Physical Oceanography, 1775-1810.

Toyooka River and National Highway Office/Kinki Regional Development Department/Ministry of Land, Infrastructure and Transport (2005): Report of investigation committee of Maruyama-river levee (in Japanese).

Ueno, T. (2005): On the occurrence mechanism of the flood disaster in the Yosasa River basin in 1998, Journal of Japan society for natural disaster science, 24-3, pp.303-321 (in Japanese).

Zhang, H., Nakagawa, H., Muto, Y. and Baba, Y. (2006): Numerical simulation of flow and local scour around hydraulic structures, Proc. of the International Conference on Fluvial Hydraulics, River Flow 2006 (in printing).

山地・河川・海岸系における物質動態に関する研究（第3報）

中川　一・関口秀雄・澤田豊明・林　泰一・山下隆男
上野鉄男・武藤裕則・馬場康之・芹澤重厚

要旨

本稿は，21世紀COEプログラムの中で「山地・河川・海岸系における物質動態に関する研究」の成果を一昨年および昨年度に引き続き第３報として取りまとめたものである。穂高砂防観測所をはじめとする隔地観測所・実験所で実施されている観測・実験を通して、山地から河川、さらに海岸・海域に至るまでの物質動態、とくに土砂動態を中心に取りまとめている。山地部では、裸地斜面からの長期的な土砂生産量を観測し、凍上・融解による土砂生産と粒度分特性が明らかになってきた。また、模型斜面を用いた豪雨時表層斜面崩壊の実験と予測モデルの検証並びに山地部での降雨・土砂流モデルの構築と観測データによる検証が行われている。水害調査にもとづく谷底平野および沖積平野における水害地形と河道変動に関する検討や、没水時の水制による局所洗掘に関する3次元流と河床変動解析法の開発も行われ、その概要が示されている。また、暴風時の沿岸流の特性や海浜風や降雨に与える黒潮などの暖流の影響などが現地観測やシミュレーションを通して明らかにされている。

キーワード: 流砂系，土砂生産，斜面崩壊，谷底平野，河道変動，地形分類図，局所洗掘，沿岸流，黒潮，MM5